THE JOURNAL OF PHYSICAL CHEMISTRY LETTERS
A JOURNAL OF THE AMERICAN CHEMICAL SOCIETY

pubs.acs.org/JPCL

Letter

Inorganic-Dominated Interphase Enabled by Tuning Solvation Configuration for 4.8 V Lithium-Ion Batteries

Haoliang Wang, Yan Zhao,* Lu Wang, Hao Zhang, Shiming Chen, Wenguang Zhao, Xiangming Yao, Yuxiang Huang, Aimin Cao, Yongli Song, Luyi Yang,* and Feng Pan*

Cite This: *J. Phys. Chem. Lett.* 2024, 15, 12234−12242

Read Online

ACCESS | Metrics & More | Article Recommendations | Supporting Information

ABSTRACT: Constructing a dense inorganic component-dominated cathode electrolyte interphase (CEI) to meet the long-term cycling requirements of ultrahigh voltage cathodes has been a crucial challenge. Nevertheless, this goal is difficult to achieve in traditional electrolyte compositions due to the inevitable decomposition of organic solvents. Herein, by utilizing the localized mismatch between the strongly coordinating hexafluorophosphate anion (PF_6^-) and the weakly coordinating solvent 1,1,1-trifluoro-*N*,*N*-dimethylmethanesulfonamide (TFDMSA), abundant aggregates (AGGs) emerged under a regular Li salt concentration of 1 m lithium bis(fluorosulfonyl)imide (LiFSI) + 0.1 m $LiPF_6$ in TFDMSA. This anion-rich Li^+ solvation structure results in an inorganic-dominated LiF-rich CEI to suppress phase transitions of lithium-rich manganese-based cathode materials (LLMO). Consequently, the prepared LLMO||Li half-cells demonstrate a capacity retention of 80.7% after 350 cycles at 4.8 V. This work advances the practical application of new electrolyte systems by proposing a new approach to construct anion-dominated Li^+ solvation structures in local environments.

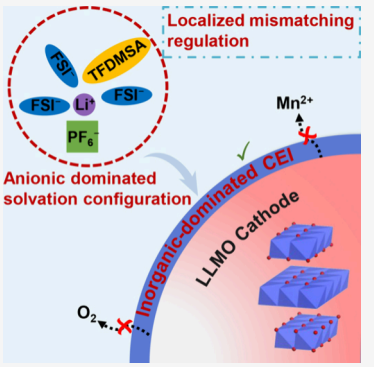

Lithium-rich manganese-based (LLMO) materials present a multitude of benefits, such as high discharge capacity, cost-efficiency, and environmental compatibility, attracting significant worldwide interest as a promising next-generation cathode candidate for high-energy-density lithium-ion batteries.[1−3] However, owing to the instability of the organic CEI formed by traditional carbonate electrolyte under high voltage as well as the presence of interfacial multiple side reactions, the LLMO displays significant voltage decay and rapid capacity fading.[4−6]

Currently, a large number of studies have focused on the anion-dominated Li^+ solvation structure to form a CEI rich in lithium fluoride (LiF) and other inorganic components. Such a CEI has excellent resistance to oxidation, inhibition of side reactions, adaptability to volume changes, and high Li^+ conductivity.[7−10] For some examples, designed by Liu et al., anchored weak solvating electrolytes (AWSEs) were derived by lengthening the chain of the polyoxymethylene ether electrolyte solvent. The $-O-CH_2-O-$ moiety in the solvent gives rise to a feeble four-membered-ring Li^+ coordination configuration. At moderate salt concentrations, the solvation structure was regulated, realizing the formation of an inorganic-rich CEI on the nickel-rich cathode ($LiNi_{0.8}Co_{0.1}Mn_{0.1}O_2$), ensuring its excellent long-term cyclic stability at 4.5 V.[11] Kim et al. investigated the weak coordination capacity of the two oxygen atoms in 1,2-bis(1,1,2,2-tetrafluoroethoxy)ethane. By combining lithium fluoromalonato(difluoro)borate with silver nitrate, they enhanced the electrode−electrolyte interface protection, subsequently improving the oxidation resistance of ether-based electrolytes.[12] However, most presently reported weakly coordinating solvents, such as 1,3-dioxolane,[13] 1,4-dioxane,[14] and tetrahydrofuran,[15] encounter challenges in meeting stable cycling requirements beyond 4.6 V. In addition, current solvation structure regulation systems with regular lithium salt concentrations are predominantly implemented in the system of LiFSI/LiTFSI in weakly coordinating solvents, which are prone to cause corrosion of Al current collectors under high voltage.[16] For commercially employed lithium hexafluorophosphate ($LiPF_6$) with the strong coordinating anion PF_6^-, weakly coordinating solvents exhibit reduced competitive potency relative to PF_6^- during the coordination with Li^+. $LiPF_6$ is able to achieve sufficient dissociation only at a relatively low concentration (substantially beneath 1 M). At the standard 1 M concentration, the insufficient dissociation of a substantial quantity of $LiPF_6$ gives rise to macroscopic insolubility, signifying a mismatch between PF_6^- and weakly coordinating solvents that restricts the practical implementation.[13−15] In recent years, highly fluorinated sulfonamide-based electrolytes have been employed for high-voltage cathodes due to their relatively high antioxidant property.[17−19] However, if only relying on the oxidation stability of the solvent itself, a significant amount of organic components are still generated,

Received: October 27, 2024
Revised: November 28, 2024
Accepted: December 2, 2024
Published: December 5, 2024

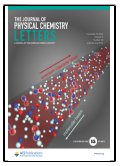

https://doi.org/10.1021/acs.jpclett.4c03094
J. Phys. Chem. Lett. 2024, 15, 12234−12242

Scheme 1. Design Concept and Mechanism of Li^+ Solvation Structure by Localized Mismatching Regulation to Form Inorganic Interphase with Action of TFDMSA-FP

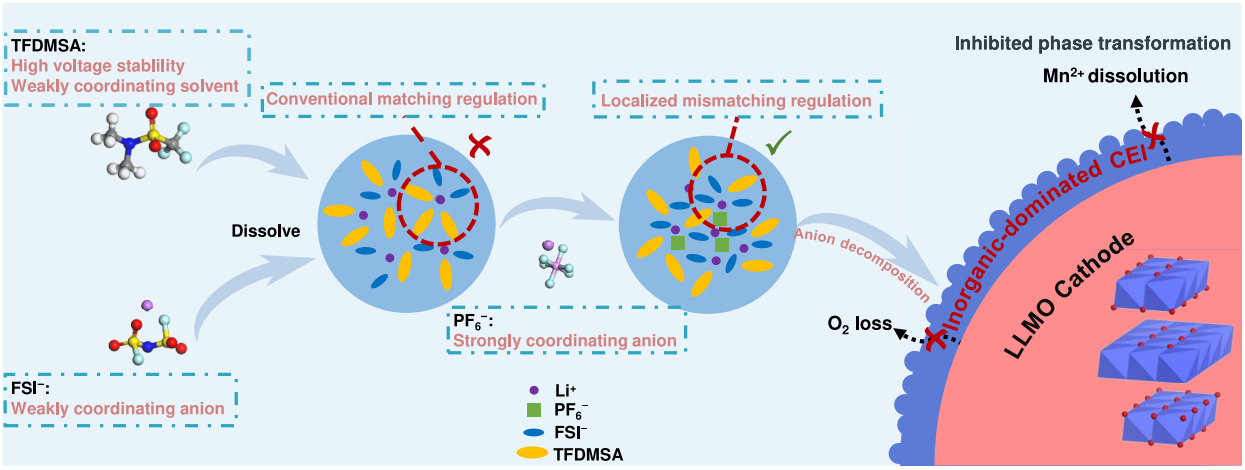

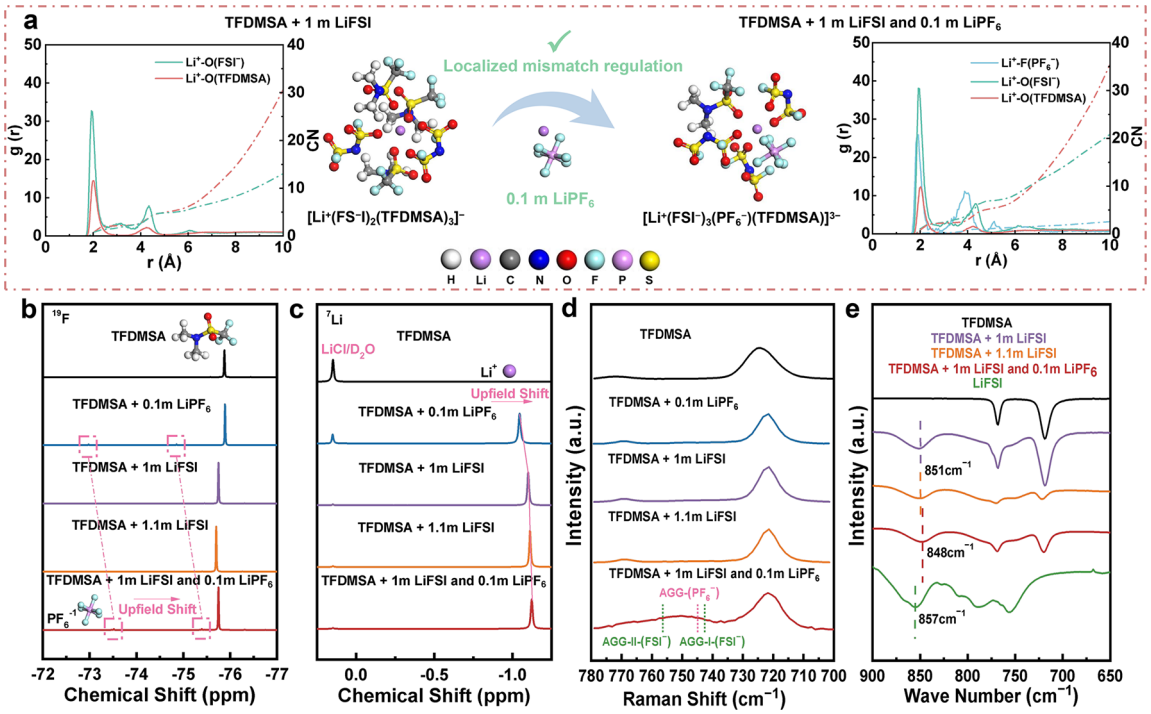

Figure 1. a) The representative solvation structure of the primary Li^+ solvation sheath, radial distribution functions (RDFs) and coordination numbers for TFDMSA + 1 m LiFSI (left) and TFDMSA-FP ((right), the abbreviation for TFDMSA + 1 m LiFSI and 0.1m $LiPF_6$). Color scheme of atoms: H-white, Li-purple, C-gray, N-dark blue, O-red, F-light blue, P-light purple, and S-yellow. b) ^{19}F-NMR, c) ^{7}Li NMR, d) Raman spectra, and e) FTIR spectra of TFDMSA solvent, different electrolytes, and lithium salts.

making it difficult to meet the requirements for long-term cycling under high voltages.[17,20] Hence, modulating the Li^+ solvation structure to give anion dominance, which further reduces the irreversible decomposition of fluorinated sulfonamide solvents, is crucial.

Herein, we stepped out of the conventional matching weakly solvating electrolyte that contains only weakly coordinating solvents and weakly coordinating anions (FSI^-/$TFSI^-$). By introducing a small quantity of the strongly coordinating anion PF_6^- (Figure S1),[21] we take advantage of the localized mismatch: the insufficient dissociation of a minimal quantity of $LiPF_6$ forming ion pairs (Scheme 1). Molecular dynamics (MD) simulations and spectroscopic results affirmed that AGGs were abundant under a regular Li salt concentration of 1 m LiFSI + 0.1 m $LiPF_6$ in TFDMSA (TFDMSA-FP, 1 m means 1 mol of Li-salt dissolved in 1 kg solvent) but were absent in the LiFSI in TFDMSA single-salt electrolyte with the same lithium-ion concentration (1.1 m). Due to the good high-voltage stability of TFDMSA itself and the preferential decomposition of AGGs in the Li^+ solvation structure, an inorganic-dominated CEI was obtained, effectively suppressing the surface phase transitions of LLMO.

First, quantum chemistry calculations were utilized to depict the coordinating ability of TFDMSA. TFDMSA's lower binding energy with Li^+ shown in Figure S1 and its less pronounced negative potential around oxygen atoms in

https://doi.org/10.1021/acs.jpclett.4c03094
J. Phys. Chem. Lett. 2024, 15, 12234−12242

electrostatic potential (ESP) maps as depicted in Figure S2 jointly unveil its weaker coordination ability than traditional carbonate solvents. Besides, $LiPF_6$ exhibits low solubility of ~0.2 m in TFDMSA (~1.5 m for LiFSI in TFDMSA) and high solvation free energy (Figure S3), indicating the relatively poor matching degree between strongly coordinating anion PF_6^- and the weakly coordinating solvent TFDMSA, thereby explaining LiFSI was employed rather than $LiPF_6$ in previous studies.[14,22] Nevertheless, by introducing a small quantity of $LiPF_6$ into LiFSI in TFDMSA,[21] a localized mismatch is engendered to form an anion-dominated solvation structure.

To detect the feasibility of the regulation strategy, we designed four colorless, transparent, and homogeneous dilute electrolytes with TFDMSA as the single solvent (Figure S4) and conducted molecular dynamics (MD) simulations. Figure S5a−d display snapshots of the solvation environment surrounding Li^+, illustrating the solvation structures in various electrolyte formulations. The representative portion of the first solvation sheath within a 3 Å range was extracted (as shown in Figure 1a and Figure S6a,b) and the coordination numbers for each constituent were displayed in Table S1. For TFDMSA + 1 m LiFSI, the weak coordination affinity between TFDMSA and Li^+ incurs a significant presence of FSI^- within the solvation sheath (CN value of 2.10). The introduction of 0.1 m $LiPF_6$ not only elevates the coordination number (CN) of FSI^- anions in TFDMSA-FP to 2.47 but also leads to the participation of PF_6^- in coordination (CN value of 0.24). The radial distribution functions (RDFs) reflect the average distance and coordination intensity of each component from the central Li-ion, as illustrated in Figures 1a and S6c,d. Particular anions and solvents nearly occupy relatively invariant positions in the four sets of electrolytes. PF_6^- and FSI^- are situated in the inner solvation sheath layer, with initial RDF peaks at 1.83 and 1.95 Å, while TFDMSA shows a peak at 2.01 Å (Table S2), indicating the weak coordination characteristic of TFDMSA. It is noted that the peak position of PF_6^- shifts notably from 1.83 Å in TFDMSA + 0.1 m $LiPF_6$ to 1.93 Å in TFDMSA-FP. This discovery arises from the competition between PF_6^- and FSI^- in the anion-rich solvation structure of Li^+. However, PF_6^- (1.93 Å) remains in a relatively more inner position than FSI^- (1.95 Å). Consequently, the presence of PF_6^- shortens the average anion-Li^+ coordination distance compared to that of pure LiFSI in TFDMSA, allowing more anions to be accommodated within the initial solvation sheath (within 3 Å) and thus forming a large number of AGGs. The analysis above reveals that TFDMSA displays distinct weak coordination with Li^+, and the localized mismatch between TFDMSA and PF_6^- facilitates the generation of an abundance of AGGs at low concentrations.

Nuclear magnetic resonance (NMR) spectroscopy was utilized to investigate the coordinated sites and solvation environment of Li^+. Figure 1b shows that the addition of 0.1 m $LiPF_6$ does not cause a notable shift in the ^{19}F peak of trifluoromethyl groups in TFDMSA, likely due to the low salt concentration. A slight downfield shift is observed in TFDMSA + LiFSI. This can be attributed to the decrease in the shielding effect around the F atom when Li^+ coordinates with the O atom in TFDMSA.[19,23] Notably, when both $LiPF_6$ (0.1 m) and LiFSI (1 m) are incorporated, the ^{19}F peak positions of PF_6^- (corresponding to approximately −73 and −75 ppm, enclosed by pink borders) exhibit a marked upfield shift.[24] This indicates that the interaction between PF_6^- and Li^+ ions was diminished by the presence of LiFSI, suggesting competition for coordination with Li^+ between FSI^- and PF_6^- in the solvation sheath, which is consistent with the above RDF analysis. ^7Li NMR was also employed, utilizing $LiCl/D_2O$ as an internal standard (Figure 1c). In comparison to the TFDMSA + 0.1 m $LiPF_6$ electrolyte, the TFDMSA + 1 m LiFSI system induces an upfield region in the ^7Li peak. This primarily stems from the improved lithium salt concentration, which was further demonstrated by the ^7Li peak shift of TFDMSA + 1.1 m LiFSI electrolyte.[25] However, the TFDMSA-FP exhibits a more prominent upfield shift than TFDMSA + 1.1 m LiFSI. The enhanced shielding effect, which is often associated with more anion coordination around Li^+, suggests that PF_6^- is capable of providing increased anion pairing.[26]

For a more in-depth exploration of anion coordination, Raman spectra were additionally examined. As shown in Figures 1d and S7, no obvious AGG formations are observed in the TFDMSA + 1 m LiFSI electrolyte. This suggests that the majority of FSI^- exist primarily as solvated separated ion pairs (SSIPs, located at ~720 cm^{-1}) and contact ion pairs (CIPs, located at ~730 cm^{-1}).[27] Upon the addition of an extra 0.1 m $LiPF_6$, significant formation of AGG-(PF_6^-) at approximately 745 cm^{-1}, AGG-I-(FSI^-), where one FSI^- coordinates with two lithium ions and is located at approximately 742 cm^{-1}, and AGG-II-(FSI^-), where one FSI^- coordinates with three lithium ions and is located at approximately 757 cm^{-1}, is observed in TFDMSA-FP.[28,29] However, such species are absent in TFDMSA + 1.1 m LiFSI. The abundance of AGGs account for the enhanced shielding effect of Li^+ as evidenced in the ^7Li NMR spectra, thereby revealing the most significant ^7Li peak shift in TFDMSA-FP. Fourier transform infrared spectroscopy (FTIR) was employed to analyze the vibrational peaks of FSI^- in different electrolytes, reflecting the effect of $LiPF_6$ on the solvation structures (Figure 1e and S8). In TFDMSA + LiFSI systems, the interaction between FSI^- with Li^+ weakens due to the dissociation of LiFSI, causing the asymmetric stretching vibration peak of the S−N−S bond in FSI^- to shift toward lower frequencies (from 857 cm^{-1} for LiFSI to 851 cm^{-1} for FSI^-).[30,31] Upon introducing $LiPF_6$, the vibration peak further shifts from 851 to 848 cm^{-1}, indicating that the interaction between Li^+ and FSI^- was further diminished.[32] The observed shift, in conjunction with the alterations in the ^{19}F peaks, implies a competitive coordination between FSI^- and PF_6^- with Li^+ within the compact inner solvation sheath. In summary, the aforementioned regulation adeptly exploits the localized mismatch to alter the solvation configuration. PF_6^- not only provides additional anion coordination other than FSI^- but also reduces the overall coordination distance between anions and Li^+, inducing the formation of AGGs in the first solvation sheath, laying a solid foundation for the formation of an inorganic CEI, which is paramount importance for the stable cycling of the LLMO cathode at ultrahigh voltages.

To explore the stability of the mentioned electrolytes under high voltages, linear sweep voltammetry (LSV) tests were initially conducted. As observed in Figure S9, the base electrolyte 1 M $LiPF_6$ in EC:DMC:EMC = 1:1:1 Vol% (EDE-P), which is a typical traditional matching strongly solvating electrolyte (the combined use of strongly coordinating anion PF_6^- and strongly coordinating solvents EC, DMC, and EMC), exhibits continuous decomposition at potentials above 4 V, which implies the instability of the conventional electrolyte system for operation under high voltage. Interestingly, the TFDMSA + 1 m LiFSI system displays a noticeable

https://doi.org/10.1021/acs.jpclett.4c03094
J. Phys. Chem. Lett. 2024, 15, 12234−12242

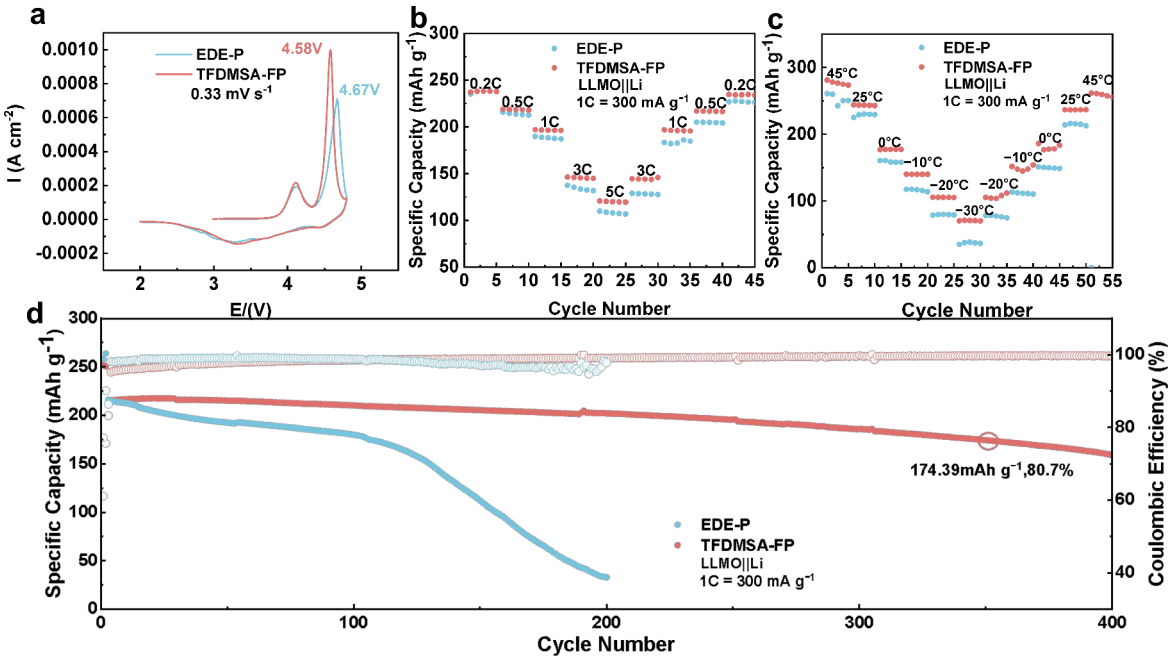

Figure 2. a) The initial cyclic voltammetry (CV) curves of Li||LLMO cells in TFDMSA-FP and EDE-P at a scanning rate of 0.33 mV s^{-1} (V vs Li/Li^+), b) rate performance of LLMO||Li cells under room temperature, and c) capacity of LLMO||Li cells at 0.33 C under a wide temperature range with the voltage range from 2 to 4.8 V (V vs Li/Li^+). d) Long-term cycling performance of LLMO||Li cells in two electrolytes with the voltage range from 2 to 4.8 V (vs Li/Li^+) at 1 C (1 C = 300 mA g^{-1}) after 2 activation cycles at 0.2 C (areal mass loading of 2.3 mg cm^{-2} in LLMO||Li half-cells).

current at low voltages (about 3.5 V), which can be attributed to the very common corrosion of aluminum current collector by low-concentration LiFSI.[16,33] The increased LiFSI concentration (1.1 m) improves oxidation resistance, characterized by observable currents at relatively higher voltages up to 3.7 V. This change can be attributed to alterations in its solvation structure due to the higher salt concentration.[27] However, TFDMSA-FP demonstrates exceptional high-voltage tolerance, with the decomposition onset potential reaching approximately 4.9 V. The corrosion induced by FSI^- is effectively suppressed, attributable to the passivation effect of PF_6^- and the formation of AGGs.[34] The formation of AGGs helps reduces the quantity of free FSI^- and form a stable CEI, thus inhibiting the dissolution of Al^{3+}.[35,36] For EDE-FP (1 m LiFSI + 0.1 m $LiPF_6$ in EC:DMC:EMC = 1:1:1 Vol%), carbonate solvents are inherently unstable at high voltages. Moreover, the strong coordinating ability of carbonate solvents excludes anions from the first solvation sheath,[14] making the localized mismatching regulation inapplicable. The prominent and persistent signal current indicates difficulty in meeting the operational requirements at high voltages. The initial CV curves of LLMO cathodes using EDE-P, EDE-FP, and TFDMSA-FP all displays two distinct oxidation peaks (Figures 2a and S10), corresponding to lithium-ion extraction from $LiMO_2$ (M = Ni, Co, Mn) at around 4.1 V and an irreversible electrochemical activation at approximately 4.6 V.[37] However, TFDMSA-FP exhibits a lower oxidation potential (4.58 V) in comparison with those in EDE-P and EDE-FP (4.67 V). This suggests that LLMO in TFDMSA-FP exhibits a smaller activation potential, thus reducing polarization losses.[38] Besides, the CV curves using TFDMSA-FP exhibit a higher degree of overlap, signifying its excellent cycling stability (Figure S11).

The electrochemical performance of the LLMO||Li half-cells assembled with TFDMSA-FP was evaluated. LLMO||Li half-cells using TFDMSA-FP show enhanced rate performance and lower-temperature performance, as shown in Figure 2b,c. This is attributed to the fast Li^+ solvation-desolvation process brought by the inorganic CEI and the lower melting point of TFDMSA (−42 °C). Under a voltage range of 2−4.8 V and a current density of 1 C (300 mA g^{-1}), a capacity retention of 80.7% was obtained after 350 cycles. In comparison, the half cells using EDE-P and EDE-FP fail within short cycles (Figures 2d and S12−S13). However, TFDMSA-FP exhibits a lower initial Coulombic efficiency (ICE) (Figure S12). This may be attributed to the formation of the effective CEI, which is analyzed in the subsequent discussions. The cells with EDE-P exhibit evident capacity fading and voltage reduction after 100, 200, and more cycles, indicating severe LLMO phase transitions.[39] In comparison, TFDMSA-FP effectively suppresses such structural evolution, promoting a higher working voltage and capacity retention rate, (Figure S12). It is worth noting that the TFDMSA-based electrolyte without $LiPF_6$ (1 and 1.1 m LiFSI) fails to complete the normal first-cycle charging. This can be attributed to the severe corrosion phenomena caused by the low concentration of FSI^- as reported previously.[16,33] Here, the concentration of LiFSI was raised to nearly saturation (1.5 m, as shown in Figure S14), exceeding the realm of dilute electrolytes discussed herein. Nevertheless, its high concentration moderately inhibits corrosion (Figure S9) and the successful facilitation of LLMO cathode operation (Figure S12). In the absence of the mismatching regulation offered by $LiPF_6$, it eventually malfunctions within several tens of cycles (Figure S13).

Based on the superior performance of TFDMSA-FP in LLMO cathodes, LLMO||Gr full coin-cells were assembled. The cells using TFDMSA-FP exhibit excellent capacity retention (300 mA g^{-1}, 2−4.75 V, 200 cycles, 80.0%), while EDE-P fail in shorter cycling periods (Figure S15a). In contrast to the relatively superior performance in LLMO||Li half-cells,

https://doi.org/10.1021/acs.jpclett.4c03094
J. Phys. Chem. Lett. 2024, 15, 12234−12242

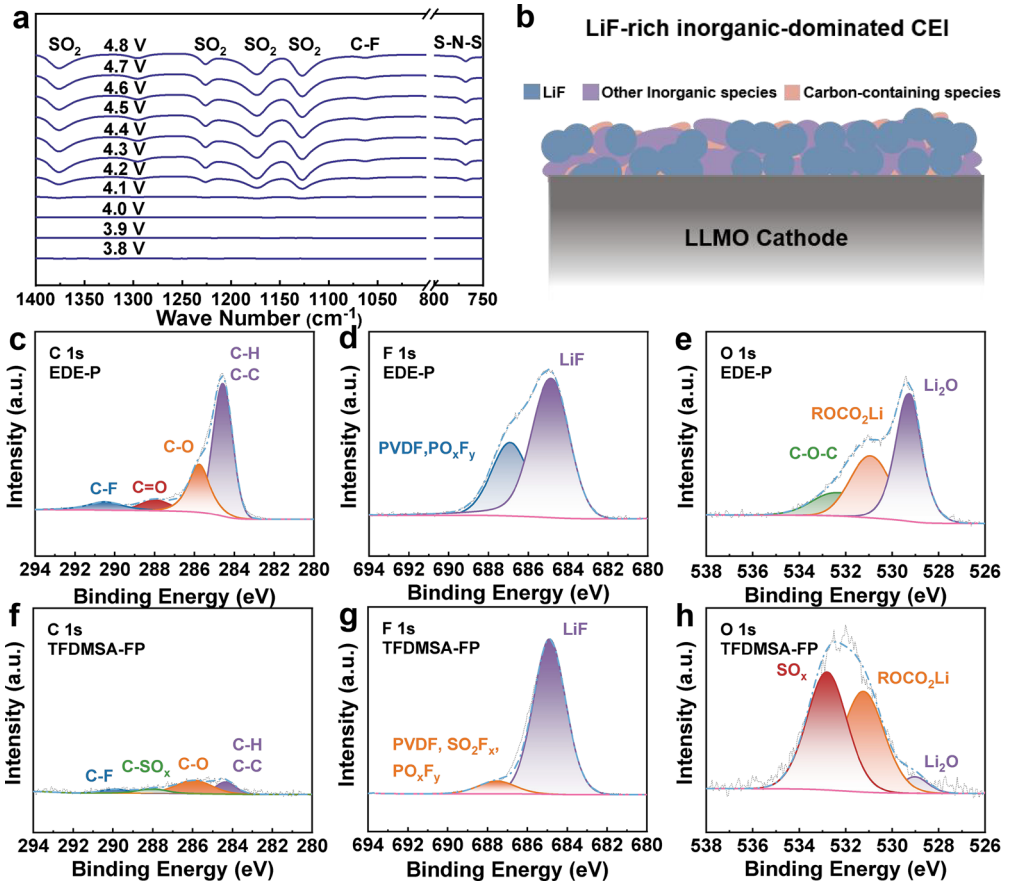

Figure 3. a) In-situ FTIR difference spectra on LLMO cathode surface during first charging process. b) Schematic diagram of the composition of LiF-rich inorganic-dominated CEI. XPS spectra of LLMO electrode surfaces subjected to 30 s etching with different electrolytes after 100 cycles (c, d, and e for EDE-P and f, g, and h for TFDMSA-FP).

the failure of the EDE-P in long-term cycling can be attributed to its slow oxidation decomposition under high voltages. The average Coulombic efficiency of EDE-P is 93.5%, which is lower than that of TFDMSA-FP (99.5%). This indicates that TFDMSA-FP possesses impressive reversibility throughout the cycling process, which is further demonstrated by substantially mitigated voltage fade (Figure S16). The excellent cycling performance is largely attributed to the stable CEI formed by TFDMSA-FP at the LLMO electrodes, ensuring the battery's reversible cycling and effectively suppressing irreversible structural degradation at the cathode end. Besides, under various rates, the TFDMSA-FP group displays superior discharge performance as expected. Even at 5 C, a capacity retention of 50.9% (equivalent to 126.8 mAh g^{-1}) relative to 0.2 C was achieved, surpassing that of EDE-P (116.3 mAh g^{-1}, 46.0%) as shown in Figure S15b. However, by measuring the ionic conductivity of the electrolyte, it is found that the ionic conductivity of TFDMSA-FP with a large number of anions in the solvation sheath is lower than that of the base electrolyte (Table S3).[40] Hence, the accelerated lithiation-delithiation process enabled by inorganic CEI plays a crucial role in enhancing the rate performance.

To elucidate the formation process and origins of the CEI, in situ FTIR was employed to investigate the interfacial evolution of the LLMO cathode surface using TFDMSA-FP during the initial charging process. From Figure 3a, it is evident that there is negligible decomposition of the surface components of the cathode material before a voltage of 4.1 V. Around 4.2 V, the emergence of the asymmetric stretching vibrations of the sulfonyl group (O═S═O) at 1376 cm^{-1} and the symmetric stretching peaks at 1226 cm^{-1}, 1173 cm^{-1}, and 1127 cm^{-1} are observed.[30,32] Additionally, the distinct symmetric stretching peak of S−N−S at 768 cm^{-1}, which is unique to FSI^{-1}, indicates that the decomposition originates from FSI^{-1}. The very faint C−F stretching vibration peak at 1063 cm^{-1}, unique to TFDMSA, suggests the minor decomposition of a small quantity of TFDMSA within the first solvation sheath.[30,41] XPS was conducted to provide more precise information about the CEI composition. The C 1s spectra display relatively weak signal peaks, implying a low content of organic components in CEI (Figure 3c,f). From an elemental standpoint, carbon atoms occupy a meager 2%, while a considerable amount of fluorine manifests in the TFDMSA-FP group (Table S4), predominantly as LiF (Figures 3d,g, and S17). The F 1s spectra indicate that TFDMSA-FP forms more lithium fluorides than EDE-P on the LLMO surface (685 eV), while the SO_2F_x arise from the partial decomposition of FSI^- and TFDMSA (Figures 3d,g and S17).[18] In the O 1s spectra, significant amounts of Li_2O are present in EDE-P both before and after etching. However, only trace amounts of Li_2O are detected in TFDMSA-FP (Figures 3e,h and S17). This can be attributed to the effective inhibition of irreversible Li_2O loss in TFDMSA-FP, especially during the first cycle, and also hints at better structural protection for LLMO. Furthermore, the evident SO_x peaks suggest the oxidation decomposition of sulfur-containing components in TFDMSA-FP, which was

https://doi.org/10.1021/acs.jpclett.4c03094
J. Phys. Chem. Lett. 2024, 15, 12234−12242

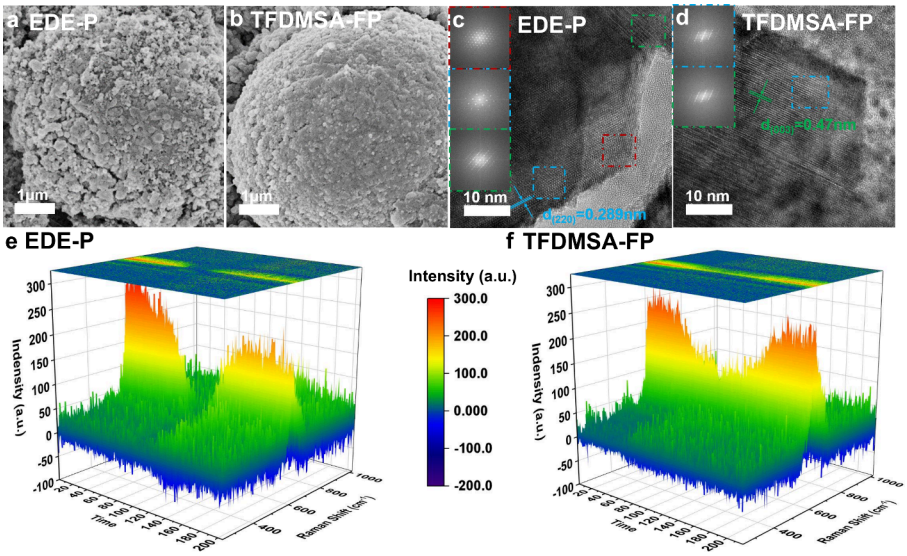

Figure 4. SEM and TEM images of LLMO electrodes disassembled from LLMO||Li cells with different electrolytes after 100 cycles, [a, c) for EDE-P, [b, d) for TFDMSA-FP]. 3D in situ Raman spectra evolution of the LLMO particles in EDE-P and TFDMSA-FP at the E_g and A_{1g} Raman active vibrational peaks during the first cycle at 0.33 mV s^{-1}, e) for EDE-P] and f) for TFDMSA-FP].

further verified by the N 1s and S 2p peaks (Figure S17−18).[20] Furthermore, the relatively higher P content in TFDMSA-FP compared to EDE-P, as indicated in Table S4, suggests the decomposition of a portion of the PF_6^- ions within the primary solvation structure. Based on the aforementioned analysis, the anion-dominated solvation structure effectively creates an inorganic CEI, which can suppress structural degradation of LLMO at high voltage operation.

X-ray diffraction (XRD) measurements were conducted to unveil the structural evolution of the LLMO cathodes after cycling. Following cycling, in LLMO, the positional exchange between Ni^{3+} at the octahedral 3(a) site and Li^+ at the 3(b) site in the space group $R\bar{3}m$ weakens the intensity of the (003) peak, while this exchange does not affect the intensity of the (104) peak. As a result, the I_{003}/I_{104} ratio reflects the degree of Li−Ni cation mixing, with I_{003}/I_{104} < 1.2 indicating severe cationic mixing.[42] As observed in Figure S19, the pristine electrodes exhibit a relatively ordered structure with an I_{003}/I_{104} ratio of 2.78. However, the I_{003}/I_{104} ratio in the cycled electrodes in EDE-P substantially decreases to 0.95, suggesting severe Li−Ni cation mixing. In contrast, the electrode in TFDMSA-FP maintains an I_{003}/I_{104} ratio of >1.29, implying a relatively better ordering. These findings underscore TFDMSA-FP's ability to suppress the otherwise inevitable structural degradation occurring during LLMO cycling. To investigate the dissolution of Mn^{2+}, inductively coupled plasma (ICP) analysis was performed (Figure S20). A substantial amount of Mn^{2+} occurs in the EDE-P group after cycling with a concentration of 0.14 mg/L. In contrast, this dissolution process is notably suppressed in the TFDMSA-FP group (0.04 mg/L). This finding indicates that TFDMSA-FP contributes to mitigating Mn^{2+} dissolution from the LLMO cathode during cycling, thereby preserving an optimal layered structure.[4]

Scanning electron microscopy (SEM) was utilized to examine the integrity of LLMO particles after cycling (Figures 4a,b and S21).[43] The images reveal that the sizes of the secondary spherical LLMO particles are similar, approximately 5−10 μm. However, the particles in EDE-P exhibit considerable cracks and a relatively irregular spherical shape after 100 cycles. The generation of these cracks might initially stem from a higher oxygen vacancy concentration causing lattice contraction, as well as the local spinel phase transformations expanding throughout the entire crystal over extended cycling periods, ultimately leading to particle fracture.[44] In contrast, TFDMSA-FP provides excellent protection for the material's integrity, resulting in barely visible, minute cracks after cycling. The preservation of the well-defined spherical structure highlights its advantage in mitigating the structural degradation of LLMO. Notably, this inhibition of phase transitions is intricately related to the robust and effective CEI in situ formed during cycling.

For a more compelling illustration of bulk phase transitions within LLMO particles, focused ion beam (FIB) and high-resolution transmission electron microscopy (HR-TEM) were employed (Figures 4c,d and S22). Through the HR-TEM pattern of the cycled LLMO particles, the near-surface region of the LLMO particle in EDE-P manifests the presence of distinct polymorphic phases, including the spinel phase and rock-salt phase (indicated by the blue and red boxes, respectively).[45] Almost no obvious layered phase is visible. These regions were also confirmed well by their corresponding fast Fourier transform (FFT) patterns. The crystal plane spacing of 0.289 nm, corresponding to the (220) crystal plane in the spinel structure, is also identified.[46] These findings suggest that EDE-P struggles to suppress phase transitions in LLMO during cycling, potentially due to poor electrolyte stability at high voltages and the insufficiently compact CEI formed. Furthermore, the irreversible phase transitions from the outer to the inner parts of the particles are in agreement with the SEM observations, revealing an abundance of cracks and even pulverization. Conversely, the phase transition in the LLMO particle using TFDMSA-FP is effectively suppressed, with the particle predominantly displaying the layered structure and only a minor presence of the spinel phase interspersed, while no apparent rock-salt phase is visible. The FFT patterns likewise corroborate this observation. Additionally, the crystal plane spacing of 0.47 nm, corresponding to the (003) crystal plane in the layered phase, is identified.[47] This

https://doi.org/10.1021/acs.jpclett.4c03094
J. Phys. Chem. Lett. 2024, 15, 12234−12242

evidence underlines the crucial role of TFDMSA-FP in mitigating structural degradation during LLMO cycling. Such inhibitory effects might originate from the fast formation of a robust and homogeneous inorganic CEI and subsequent suppressed surface phase transitions of the LLMO.

In situ Raman characterization was further conducted to gain a clearer and more direct observation of the evolution of the crystal structure during the initial charge−discharge process, as shown in Figure 4e,f. Before charging, the pristine LLMO at the open-circuit potential (OCP) exhibits the typical E_g and A_{1g} bands in the Raman spectrum, which correspond to vibrations at 490 cm^{-1} and stretching at 605 cm^{-1}, respectively. The peak at 430 cm^{-1} is associated with the monoclinic Li_2MnO_3 structure (Figure S23).[4] As the voltage continuously increases, a noticeable decrease in the peak intensities of both the E_g and A_{1g} modes is observed for both samples, indicating weakened O-TM-O and TM-O bonds at high voltage. As the CV undergoes a negative sweep, peak intensities in the TFDMSA-FP group almost fully recover to their initial states, while the EDE-P group exhibits a substantial attenuation compared to the initial intensity, corresponding to the destruction of the layered structure.[48]

In this work, we aim to construct an inorganic-dominated CEI for high-voltage LLMO cathode by utilizing the localized mismatch between the strongly coordinating anion PF_6^- and the weakly coordinating solvent TFDMSA. By introducing 0.1 m $LiPF_6$ to 1 m LiFSI in TFDMSA, large amounts of AGGs emerged, forming a robust CEI consists of LiF, SO_x, phosphides and nitrides, etc. Benefiting from this CEI, irreversible degradation of LLMO was suppressed. Consequently, the stable operation of LLMO was achieved at a high voltage of 4.8 V (80.7% capacity retention after 350 cycles). Besides, proof-of-concept LLMO||Gr full cells also exhibit improved cycling performance (200 cycles, 80% capacity retention) and enhanced rate performance. In brief, this new design approach for regulating solvation structures has successfully opened up new avenues for the practical application of nonconventional high-voltage lithium-ion battery electrolytes.

■ ASSOCIATED CONTENT

Supporting Information

The Supporting Information is available free of charge at https://pubs.acs.org/doi/10.1021/acs.jpclett.4c03094.

Experimental Section/Methods, Characterizations, Computational Details, Figures, Tables, etc. (PDF)

■ AUTHOR INFORMATION

Corresponding Authors

Yan Zhao − *School of Advanced Materials, Peking University Shenzhen Graduate School, Shenzhen 518055, China; School of Energy and Power Engineering, Jiangsu University, Zhenjiang 212013, China*; Email: zhaoyan@ujs.edu.cn

Luyi Yang − *School of Advanced Materials, Peking University Shenzhen Graduate School, Shenzhen 518055, China*; orcid.org/0000-0002-5516-9829; Email: yangly@pkusz.edu.cn

Feng Pan − *School of Advanced Materials, Peking University Shenzhen Graduate School, Shenzhen 518055, China*; orcid.org/0000-0002-8216-1339; Email: panfeng@pkusz.edu.cn

Authors

Haoliang Wang − *School of Advanced Materials, Peking University Shenzhen Graduate School, Shenzhen 518055, China*

Lu Wang − *School of Advanced Materials, Peking University Shenzhen Graduate School, Shenzhen 518055, China*

Hao Zhang − *School of Advanced Materials, Peking University Shenzhen Graduate School, Shenzhen 518055, China*

Shiming Chen − *School of Advanced Materials, Peking University Shenzhen Graduate School, Shenzhen 518055, China*

Wenguang Zhao − *School of Advanced Materials, Peking University Shenzhen Graduate School, Shenzhen 518055, China*

Xiangming Yao − *School of Advanced Materials, Peking University Shenzhen Graduate School, Shenzhen 518055, China*

Yuxiang Huang − *School of Advanced Materials, Peking University Shenzhen Graduate School, Shenzhen 518055, China*

Aimin Cao − *School of Advanced Materials, Peking University Shenzhen Graduate School, Shenzhen 518055, China*

Yongli Song − *School of Energy and Power Engineering, Jiangsu University, Zhenjiang 212013, China*; orcid.org/0000-0003-2231-2438

Complete contact information is available at: https://pubs.acs.org/10.1021/acs.jpclett.4c03094

Notes

The authors declare no competing financial interest.

■ ACKNOWLEDGMENTS

This work was kindly supported by Research Foundation for Advanced Talents of Jiangsu University, China (Grant No. 23JDG041), The Major Science and Technology Infrastructure Project of Material Genome Big-science Facilities Platform supported by Municipal Development and Reform Commission of Shenzhen, The Major Science and Technology Infrastructure Project of Material Genome Big-science Facilities Platform supported by Municipal Development and Reform Commission of Shenzhen, Basic and Applied Basic Research Foundation of Guangdong Province (No. 2021B1515130002), International joint Research Center for Electric Vehicle Power Battery and Materials (No. 2015B01015), Guangdong Key Laboratory of Design and calculation of New Energy Materials (No. 2017B030301013), Shenzhen Key Laboratory of New Energy Resources Genome Preparation and Testing (No. ZDSYS201707281026184), and Shenzhen Science and Technology Planning Project (JSGG20220831095604008).

■ REFERENCES

(1) Zhu, W.; Zhang, J. C.; Luo, J. W.; Zeng, C. H.; Su, H.; Zhang, J. F.; Liu, R.; Hu, E. Y.; Liu, Y. S.; Liu, W. D.; Chen, Y. A.; Hu, W. B.; Xu, Y. H. Ultrafast Non-Equilibrium Synthesis of Cathode Materials for Li-Ion Batteries. *Adv. Mater.* **2023**, *35*, No. 2208974.

(2) Li, X.; Qiao, Y.; Guo, S. H.; Xu, Z. M.; Zhu, H.; Zhang, X. Y.; Yuan, Y.; He, P.; Ishida, M.; Zhou, H. S. Direct Visualization of the Reversible O^{2-}/O Redox Process in Li-Rich Cathode Materials. *Adv. Mater.* **2018**, *30*, No. 1705197.

(3) He, D. Y.; Tong, W. X.; Zhang, J.; Huang, Z. Y.; Chen, Z. W.; Yang, M. L.; Wang, R.; Zhao, W. G.; Ma, Z. W.; Xiao, Y. G. Structural

insights into lithium-deficient type Li-rich layered oxide for high-performance cathode. *Chin. J. Struct. Chem.* **2023**, *42*, No. 100060.
(4) Huang, W.; Lin, C.; Qiu, J.; Li, S.; Chen, Z.; Chen, H.; Zhao, W.; Ren, G.; Li, X.; Zhang, M.; Pan, F. Delocalized Li@Mn_6 superstructure units enable layer stability of high-performance Mn-rich cathode materials. *Chem.* **2022**, *8*, 2163−2178.
(5) Lee, J.; Gong, Y.; Gu, L.; Kang, B. Long-Term Cycle Stability Enabled by the Incorporation of Ni into Li_2MnO_3 Phase in the Mn-Based Li-Rich Layered Materials. *Acs Energy Lett.* **2021**, *6*, 789−798.
(6) Arifiadi, A.; Demelash, F.; Brake, T.; Lechtenfeld, C.; Klein, S.; Alsheimer, L.; Wiemers-Meyer, S.; Winter, M.; Kasnatscheew, J. Elucidating the Limit of Lithium Difluorophosphate Electrolyte Additive for High-Voltage Li/Mn-Rich Layered Oxide || Graphite Li Ion Batteries. *Energy Environ. Mater.* **2024**, No. e12835.
(7) Wang, Q. D.; Yao, Z. P.; Zhao, C. L.; Verhallen, T.; Tabor, D. P.; Liu, M.; Ooms, F.; Kang, F. Y.; Aspuru-Guzik, A.; Hu, Y. S.; Wagemaker, M.; Li, B. H. Interface chemistry of an amide electrolyte for highly reversible lithium metal batteries. *Nat. Commun.* **2020**, *11*, 4188.
(8) Bolloju, S.; Chiou, C.-Y.; Vikramaditya, T.; Lee, J.-T. (Pentafluorophenyl)diphenylphosphine as a dual-functional electrolyte additive for $LiNi_{0.5}Mn_{1.5}O_4$ cathodes in high-voltage lithium-ion batteries. *Electrochim. Acta* **2019**, *299*, 663−671.
(9) Wang, M. W.; Sun, Q. T.; Liu, Y.; Yan, Z. A.; Xu, Q. Y.; Wu, Y. C.; Cheng, T. Impact of lithium nitrate additives on the solid electrolyte interphase in lithium metal batteries. *Chin. J. Struct. Chem.* **2024**, *43*, No. 100203.
(10) Fan, W. J.; Wang, H. L.; Wu, J. Y. Sustainable nanostructured electrolyte additives for stable metal anodes. *Escience* **2024**, *4*, No. 100248.
(11) Liu, X.; Zhang, J. W.; Yun, X. Y.; Li, J.; Yu, H. Q.; Peng, L. Q.; Xi, Z. H.; Wang, R. H.; Yang, L.; Xie, W.; Chen, J.; Zhao, Q. Anchored Weakly-Solvated Electrolytes for High-Voltage and Low-Temperature Lithium-ion Batteries. *Angew. Chem., Int. Ed.* **2024**, *63*, No. e202406596.
(12) Kim, S.; Lee, J. A.; Lee, T. K.; Baek, K.; Kim, J.; Kim, B.; Byun, J. H.; Lee, H. W.; Kang, S. J.; Choi, J. A.; Lee, S. Y.; Choi, M. H.; Lee, J. H.; Choi, N. S. Wide-temperature-range operation of lithium-metal batteries using partially and weakly solvating liquid electrolytes. *Energy Environ. Sci.* **2023**, *16*, 5108−5122.
(13) Sun, C. C.; Ji, X.; Weng, S. T.; Li, R. H.; Huang, X. T.; Zhu, C. N.; Xiao, X. Z.; Deng, T.; Fan, L. W.; Chen, L. X.; Wang, X. F.; Wang, C. S.; Fan, X. L. 50C Fast-Charge Li-Ion Batteries using a Graphite Anode. *Adv. Mater.* **2022**, *34*, No. 2206020.
(14) Yao, Y. X.; Chen, X.; Yan, C.; Zhang, X. Q.; Cai, W. L.; Huang, J. Q.; Zhang, Q. Regulating Interfacial Chemistry in Lithium-Ion Batteries by a Weakly Solvating Electrolyte**. *Angew. Chem., Int. Ed.* **2021**, *60*, 4090−4097.
(15) Zhang, J. M.; Li, Q. P.; Zeng, Y. P.; Tang, Z.; Sun, D.; Huang, D.; Tang, Y. G.; Wang, H. Y. Weakly Solvating Cyclic Ether Electrolyte for High-Voltage Lithium Metal Batteries. *Acs Energy Lett.* **2023**, *8*, 1752−1761.
(16) Zhang, X. Q.; Chen, X.; Hou, L. P.; Li, B. Q.; Cheng, X. B.; Huang, J. Q.; Zhang, Q. Regulating Anions in the Solvation Sheath of Lithium Ions for Stable Lithium Metal Batteries. *Acs Energy Lett.* **2019**, *4*, 411−416.
(17) Xue, W. J.; Shi, Z.; Huang, M. J.; Feng, S. T.; Wang, C.; Wang, F.; Lopez, J.; Qiao, B.; Xu, G. Y.; Zhang, W. X.; Dong, Y. H.; Gao, R.; Shao-Horn, Y.; Johnson, J. A.; Li, J. FSI-inspired solvent and "full fluorosulfonyl" electrolyte for 4 V class lithium-metal batteries. *Energy Environ. Sci.* **2020**, *13*, 212−220.
(18) Xue, W. J.; Huang, M. J.; Li, Y. T.; Zhu, Y. G.; Gao, R.; Xiao, X. H.; Zhang, W. X.; Li, S. P.; Xu, G. Y.; Yu, Y.; Li, P.; Lopez, J.; Yu, D. W.; Dong, Y. H.; Fan, W. W.; Shi, Z.; Xiong, R.; Sun, C. J.; Hwang, I.; Lee, W. K.; Shao-Horn, Y.; Johnson, J. A.; Li, J. Ultra-high-voltage Ni-rich layered cathodes in practical Li metal batteries enabled by a sulfonamide-based electrolyte. *Nat. Energy* **2021**, *6*, 495−505.
(19) Feng, S. T.; Huang, M. J.; Lamb, J. R.; Zhang, W. X.; Tatara, R.; Zhang, Y. R.; Zhu, Y. G.; Perkinson, C. F.; Johnson, J. A.; Shao-Horn, Y. Molecular Design of Stable Sulfamide- and Sulfonamide-Based Electrolytes for Aprotic Li-O_2 Batteries. *Chem.* **2019**, *5*, 2630−2641.
(20) Xue, W. J.; Gao, R.; Shi, Z.; Xiao, X. H.; Zhang, W. X.; Zhang, Y. R.; Zhu, Y. G.; Waluyo, I.; Li, Y.; Hill, M. R.; Zhu, Z.; Li, S.; Kuznetsov, O.; Zhang, Y. M.; Lee, W. K.; Hunt, A.; Harutyunyan, A.; Shao-Horn, Y.; Johnson, J. A.; Li, J. Stabilizing electrode-electrolyte interfaces to realize high-voltage Li||$LiCoO_2$ batteries by a sulfonamide-based electrolyte. *Energy Environ. Sci.* **2021**, *14*, 6030−6040.
(21) Zhao, Y. M.; Hu, Z. L.; Zhao, Z. F.; Chen, X. L.; Zhang, S.; Gao, J.; Luo, J. Y. Strong Solvent and Dual Lithium Salts Enable Fast-Charging Lithium-Ion Batteries Operating from-78 to 60 °C. *J. Am. Chem. Soc.* **2023**, *145*, 22184−22193.
(22) Liao, Y.; Zhou, M.; Yuan, L.; Huang, K.; Wang, D.; Han, Y.; Meng, J.; Zhang, Y.; Li, Z.; Huang, Y. Eco-Friendly Tetrahydropyran Enables Weakly Solvating "4S" Electrolytes for Lithium-Metal Batteries. *Adv. Energy Mater.* **2023**, *13*, No. 2301477.
(23) Mo, Y. B.; Liu, G. P.; Yin, Y.; Tao, M. M.; Chen, J. W.; Peng, Y.; Wang, Y. G.; Yang, Y.; Wang, C. X.; Dong, X. L.; Xia, Y. Y. Fluorinated Solvent Molecule Tuning Enables Fast-Charging and Low-Temperature Lithium-Ion Batteries. *Adv. Energy Mater.* **2023**, *13*, No. 2301285.
(24) Jiang, H. Z.; Han, X. Q.; Du, X. F.; Chen, Z.; Lu, C. L.; Li, X. T.; Zhang, H. R.; Zhao, J. W.; Han, P. X.; Cui, G. L. A PF_6− Permselective Polymer Electrolyte with Anion Solvation Regulation Enabling Long-Cycle Dual-Ion Battery. *Adv. Mater.* **2022**, *34*, 202108665.
(25) Mo, Y. B.; Liu, G. P.; Chen, J. W.; Zhu, X.; Peng, Y.; Wang, Y. G.; Wang, C. X.; Dong, X. L.; Xia, Y. Y. Unraveling the temperature-responsive solvation structure and interfacial chemistry for graphite anodes. *Energy Environ. Sci.* **2024**, *17*, 227−237.
(26) Park, E.; Park, J.; Lee, K.; Zhao, Y.; Zhou, T. H.; Park, G.; Jeong, M. G.; Choi, M.; Yoo, D. J.; Jung, H. G.; Coskun, A.; Choi, J. W. Exploiting the Steric Effect and Low Dielectric Constant of 1,2-Dimethoxypropane for 4.3 V Lithium Metal Batteries. *Acs Energy Lett.* **2023**, *8*, 179−188.
(27) Efaw, C. M.; Wu, Q. S.; Gao, N. S. J.; Zhang, Y. G.; Zhu, H. Y.; Gering, K.; Hurley, M. F.; Xiong, H.; Hu, E. Y.; Cao, X.; Xu, W.; Zhang, J. G.; Dufek, E. J.; Xiao, J.; Yang, X. Q.; Liu, J.; Qi, Y.; Li, B. Localized high-concentration electrolytes get more localized through micelle-like structures. *Nat. Mater.* **2023**, *22*, 1531−1539.
(28) Qin, K. Q.; Li, S.; Yen, D.; Zhang, W. R.; Yang, Z. Z.; Kamphaus, E. P.; Kim, E. Y.; Huang, J. H.; Shea, J. J.; Hu, E. Y.; Cheng, L.; Wang, C. S.; Luo, C. A Coordinated-Anion-Enriched Electrolyte for Lean-Electrolyte Li-S Batteries. *Acs Energy Lett.* **2024**, *9*, 4524−4525.
(29) Su, L. S.; Zhao, X. H.; Yi, M.; Charalambous, H.; Celio, H.; Liu, Y. Y.; Manthiram, A. Uncovering the Solvation Structure of LiPF6-Based Localized Saturated Electrolytes and Their Effect on $LiNiO_2$-Based Lithium-Metal Batteries. *Adv. Energy Mater.* **2022**, *12*, No. 2201911.
(30) Kerner, M.; Plylahan, N.; Scheers, J.; Johansson, P. Thermal stability and decomposition of lithium bis(fluorosulfonyl)imide (LiFSI) salts. *Rsc Advances* **2016**, *6*, 23327−23334.
(31) Beran, M.; Príhoda, J.; Zák, Z.; Cerník, M. A new route to the syntheses of alkali metal bis(fluorosulfuryl)imides: Crystal structure of $LiN(SO_2F)_2$. *Polyhedron.* **2006**, *25*, 1292−1298.
(32) Huang, J. H.; Hollenkamp, A. F. Thermal Behavior of Ionic Liquids Containing the FSI Anion and the Li^+ Cation. *J. Phys. Chem. C* **2010**, *114*, 21840−21847.
(33) Li, C. L.; Zeng, S. W.; Wang, P.; Li, Z. J.; Yang, L.; Zhao, D. N.; Wang, J.; Liu, H. N.; Li, S. Y. Mechanism of aluminum corrosion in LiFSI-based electrolyte at elevated temperatures. *Trans. Nonferrous Met. Soc. China* **2021**, *31*, 1439−1451.
(34) Han, C. X.; Chen, G. S.; Ma, Y.; Ma, J.; Shui, X.; Dong, S. M.; Xu, G. J.; Zhou, X. H.; Cui, Z. L.; Qiao, L. X.; Cui, G. L. Strategies towards inhibition of aluminum current collector corrosion in lithium batteries. *Energy Mater-Us* **2023**, *3*, 300052.

https://doi.org/10.1021/acs.jpclett.4c03094
J. Phys. Chem. Lett. 2024, 15, 12234−12242

(35) Zhang, X. R.; Dong, X. B.; Yue, X. Y.; Gao, J. Y.; Shi, Z. Q.; Liu, J. J.; Dong, Y. T.; Chen, Y. M.; Fang, M. M.; Yu, H. G.; Liang, Z. Solvation Regulation via Hydrogen Bonding to Mitigate Al Current Collector Corrosion for High-Voltage Li-Ion Batteries. *Adv. Energy Mater.* **2024**, No. 2403588.
(36) Chai, D. D.; Yan, H. T.; Wang, X.; Li, X.; Fu, Y. Z. Retuning Solvating Ability of Ether Solvent by Anion Chemistry toward 4.5 V Class Li Metal Battery. *Adv. Funct. Mater.* **2024**, *34*, No. 2310516.
(37) Song, D. P.; Yang, Z. W.; Zhao, Q.; Sun, X. L.; Wu, Y.; Zhang, Y.; Gao, J.; Wang, C.; Yang, L.; Ohsaka, T.; Matsumoto, F.; Wu, J. F. Dilute Electrolyte to Mitigate Capacity Decay and Voltage Fading of Co-Free Li-Rich Cathode for Next-Generation Li-Ion Batteries. *Acs Appl. Mater. Inter.* **2022**, *14*, 12264−12275.
(38) Shi, J. L.; Xiao, D. D.; Ge, M. Y.; Yu, X. Q.; Chu, Y.; Huang, X. J.; Zhang, X. D.; Yin, Y. X.; Yang, X. Q.; Guo, Y. G.; Gu, L.; Wan, L. J. High-Capacity Cathode Material with High Voltage for Li-Ion Batteries. *Adv. Mater.* **2018**, *30*, No. 1705575.
(39) Huang, W. Y.; Yang, L. Y.; Chen, Z. F.; Liu, T. C.; Ren, G. X.; Shan, P. Z.; Zhang, B. W.; Chen, S. M.; Li, S. N.; Li, J. Y.; Lin, C.; Zhao, W. G.; Qiu, J. M.; Fang, J. J.; Zhang, M. J.; Dong, C.; Li, F.; Yang, Y.; Sun, C. J.; Ren, Y.; Huang, Q. Z.; Hou, G. J.; Dou, S. X.; Lu, J.; Amine, K.; Pan, F. Elastic Lattice Enabling Reversible Tetrahedral Li Storage Sites in a High-Capacity Manganese Oxide Cathode. *Adv. Mater.* **2022**, *34*, No. 2202745.
(40) Xu, J. J.; Zhang, J. X.; Pollard, T. P.; Li, Q. D.; Tan, S.; Hou, S. Y.; Wan, H. L.; Chen, F.; He, H. X.; Hu, E. Y.; Xu, K.; Yang, X. Q.; Borodin, O.; Wang, C. S. Electrolyte design for Li-ion batteries under extreme operating conditions. *Nature* **2023**, *614*, 694−700.
(41) Olana, B. N.; Adem, L. H.; Lin, S. D.; Hwang, B. J.; Hsieh, Y. C.; Brunklaus, G.; Winter, M. In Situ Diffuse Reflectance Infrared Fourier-Transform Spectroscopy Investigation of Fluoroethylene Carbonate and Lithium Difluorophosphate Dual Additives in SEI Formation over Cu Anode. *Acs Appl. Energy Mater.* **2023**, *6*, 4800−4809.
(42) Li, B.; Rousse, G.; Zhang, L.; Avdeev, M.; Deschamps, M.; Abakumov, A. M.; Tarascon, J.-M. Constructing "Li-rich Ni-rich" oxide cathodes for high-energy-density Li-ion batteries. *Energy Environ. Sci.* **2023**, *16*, 1210−1222.
(43) Huang, Y.; Ji, Y.; Zheng, G.; Cao, H.; Xue, H.; Yao, X.; Wang, L.; Chen, S.; Yin, Z.; Pan, F.; Yang, L. Tailored Interphases Construction for Enhanced Si Anode and Ni-Rich Cathode Performance in Lithium-Ion Batteries. *CCS Chemistry Just Accepted* **2024**, No. 202404120.
(44) Cao, B.; Li, T. Y.; Zhao, W. G.; Yin, L.; Cao, H. B.; Chen, D.; Li, L. X.; Pan, F.; Zhang, M. J. Correlating Rate-Dependent Transition Metal Dissolution between Structure Degradation in Li-Rich Layered Oxides. *Small* **2023**, *19*, No. 2301834.
(45) Liu, T.; Liu, J.; Li, L.; Yu, L.; Diao, J.; Zhou, T.; Li, S.; Dai, A.; Zhao, W.; Xu, S.; Ren, Y.; Wang, L.; Wu, T.; Qi, R.; Xiao, Y.; Zheng, J.; Cha, W.; Harder, R.; Robinson, I.; Wen, J.; Lu, J.; Pan, F.; Amine, K. Origin of structural degradation in Li-rich layered oxide cathode. *Nature* **2022**, *606*, 305−312.
(46) Lun, Z. Y.; Ouyang, B.; Kwon, D. H.; Ha, Y.; Foley, E. E.; Huang, T. Y.; Cai, Z. J.; Kim, H.; Balasubramanian, M.; Sun, Y. Z.; Huang, J. P.; Tian, Y. S.; Kim, H.; McCloskey, B. D.; Yang, W. L.; Clément, R. J.; Ji, H. W.; Ceder, G. Cation-disordered rocksalt-type high-entropy cathodes for Li-ion batteries. *Nat. Mater.* **2021**, *20*, 214−221.
(47) Zhang, M. J.; Li, Z. B.; Yu, L.; Kong, D. F.; Li, Y. W.; Cao, B.; Zhao, W. G.; Wen, J. G.; Pan, F. Enhanced long-term cyclability in Li-Rich layered oxides by electrochemically constructing a $Li_xTM_{3-x}O_4$-type spinel shell. *Nano Energy* **2020**, *77*, No. 105188.
(48) Huang, H.; Li, Z.; Gu, S.; Bian, J.; Li, Y.; Chen, J.; Liao, K.; Gan, Q.; Wang, Y.; Wu, S.; Wang, Z.; Luo, W.; Hao, R.; Wang, Z.; Wang, G.; Lu, Z. Dextran Sulfate Lithium as Versatile Binder to Stabilize High-Voltage $LiCoO_2$ to 4.6 V. *Adv. Energy Mater.* **2021**, *11*, No. 2101864.

https://doi.org/10.1021/acs.jpclett.4c03094
J. Phys. Chem. Lett. 2024, 15, 12234−12242